ADVANCED MATERIALS
www.advmat.de

Underpotential Deposition of 3D Transition Metals: Versatile Electrosynthesis of Single-Atom Catalysts on Oxidized Carbon Supports

*Aidan Francis Meese, Cade Napier, David J. Kim, Kali Rigby, Tayler Hedtke, Denis Leshchev, Eli Stavitski, Lucas R. Parent, and Jae-Hong Kim**

Use of single-atom catalysts (SACs) has become a popular strategy for tuning activity and selectivity toward specific pathways. However, conventional SAC synthesis methods require high temperatures and pressures, complicated procedures, and expensive equipment. Recently, underpotential deposition (UPD) has been investigated as a promising alternative, yielding high-loading SAC electrodes under ambient conditions and within minutes. Yet only few studies have employed UPD to synthesize SACs, and all have been limited to UPD of Cu. In this work, a flexible UPD approach for synthesis of mono- and bi-metallic Cu, Fe, Co, and Ni SACs directly on oxidized, commercially available carbon electrodes is reported. The UPD mechanism is investigated using in situ X-ray absorption spectroscopy and, finally, the catalytic performance of a UPD-synthesized Co SAC is assessed for electrochemical nitrate reduction to ammonia. The findings expand upon the usefulness and versatility of UPD for SAC synthesis, with hopes of enabling future research toward realization of fast, reliable, and fully electrified SAC synthesis processes.

1. Introduction

Single-atom catalysts (SACs) have attracted attention across a range of disciplines in catalysis, owing to their unique, unsaturated coordination environments and strong metal-substrate interactions.[1–6] Yet, reliable synthesis of SACs remains challenging due to the high surface free energy of isolated metal atoms, which favors aggregation under conditions of typical syntheses and applications.[7,8] A variety of synthesis techniques have been developed in the literature, but many leading methods require the use of high temperature and pressure,[9–14] inert gas environment,[15–18] and/or expensive equipment,[19–21] as well as lengthy procedures and reaction times.

Electrochemical approaches to SAC synthesis offer a promising alternative, since they can be performed under ambient conditions and on the scale of minutes.[22–24] However, the large overpotentials at which electrodeposition is typically performed render it difficult to prevent formation of metal-metal bonds.[25,26] To address this problem, Xia et al. were the first to explore the use of underpotential deposition (UPD) for "self-terminating" synthesis of Cu SACs.[23] Unlike traditional electrodeposition, UPD is performed at potentials positive of or equal to a metal precursor's standard reduction potential (SRP), i.e., where reductive formation of metal-metal bonds is thermodynamically forbidden. Instead, metal atoms undergo electrosorption and/or reduction onto suitable anchor-sites of the substrate, such as nonmetal dopants, lattice defects, and vacancies.[27,28]

UPD of one metal onto a foreign metal substrate (i.e., a bulk metal electrode) has been a subject of research for decades, finding use in niche applications such as stripping voltammetry and electroplating.[29–33] However, few publications have applied UPD as a strategy for synthesis of SACs supported on nonmetal substrates. These include the synthesis of Cu SACs supported on transition metal dichalcogenides followed by galvanic displacement of Cu with noble metals,[23] and the synthesis of copper SACs on sulfur-doped graphite foam.[34] While these studies demonstrate the promise of UPD-based strategies for synthesis of Cu SACs, questions remain as to the precise mechanism of UPD on nonmetal substrates and its ability to form SACs of metals less noble than Cu.

In this work, we present a versatile, one-step UPD-based SAC synthesis protocol to deposit a variety of transition metals, e.g., Cu, Fe, Co, and Ni directly onto oxidized carbon electrodes, without use of inks or binders (**Figure 1a**). We then extend this protocol for the first time to obtain bi-metallic SACs and

A. F. Meese, C. Napier, D. J. Kim, K. Rigby, T. Hedtke, J.-H. Kim
Department of Chemical & Environmental Engineering
Yale University
New Haven CT 06520, USA
E-mail: jaehong.kim@yale.edu
D. Leshchev, E. Stavitski
National Synchrotron Light Source II
Brookhaven National Laboratory
Upton, NY 11973, USA
L. R. Parent
Innovation Partnership Building
University of Connecticut
159 Discovery Dr., Storrs, CT 06269, USA

The ORCID identification number(s) for the author(s) of this article can be found under https://doi.org/10.1002/adma.202311341

DOI: 10.1002/adma.202311341

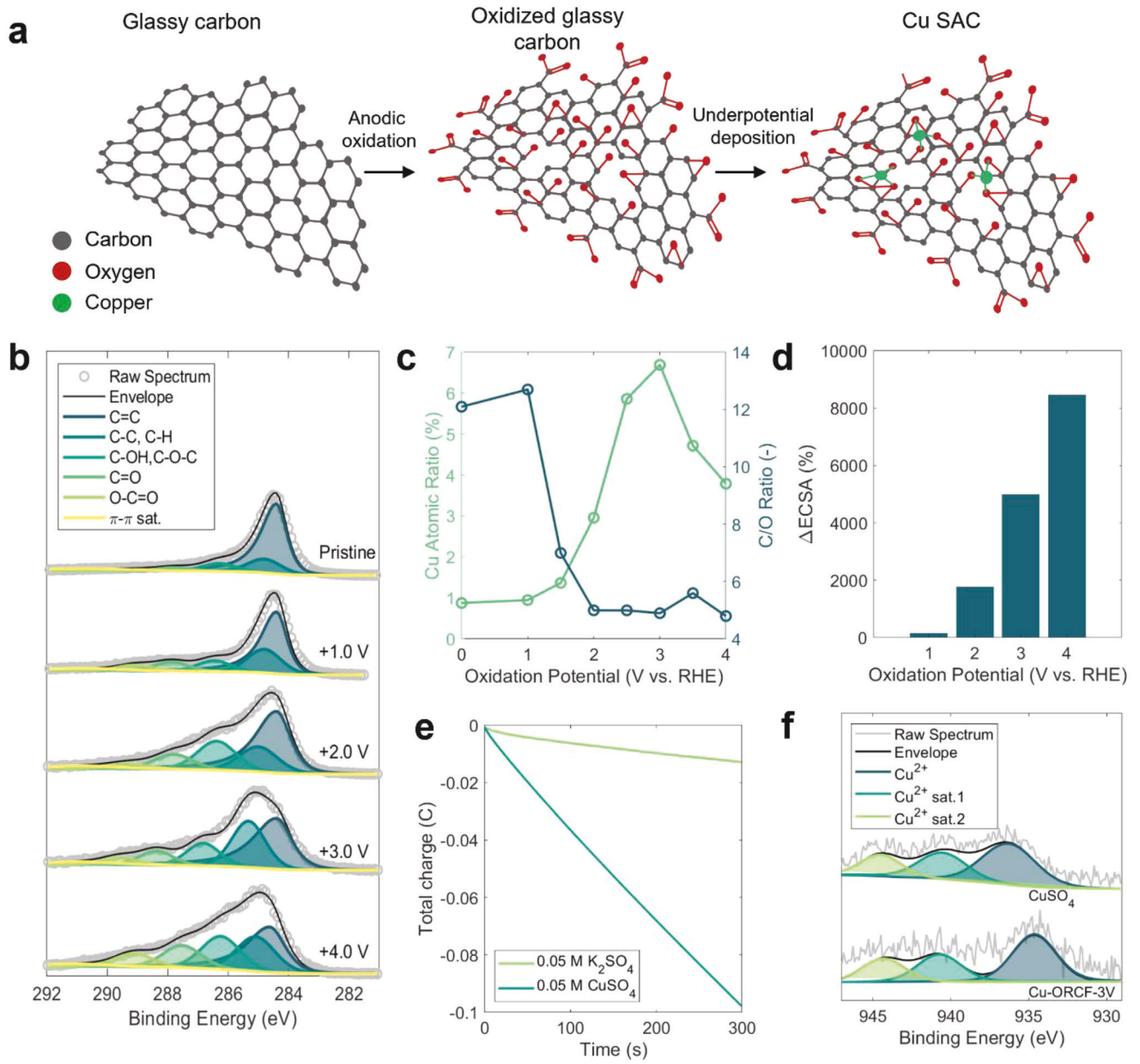

Figure 1. Overview of SAC synthesis approach and characterization of oxidized carbon substrates. a) illustration of key steps in UPD-based SAC synthesis approach. b) Normalized C1s XPS spectra of pristine RCF and ORCF substrates (key entries are in descending order from low to high binding energy). Six peaks were fitted to each C1s spectrum, corresponding to C═C (248.5 eV), C—C, C—H (285.0 eV), C—OH, C—O—C (286.5 eV), C═O (287.9 eV), O—C═O (288.8 eV), and π–π^* satellite (291.6 eV).[41] c) Relative Cu atomic ratio and C/O ratio of RCF and ORCF substrates as functions of oxidation potential, estimated using XPS. d) Change in ECSA for ORCF substrates following oxidation at various potentials, as determined from DLC measurements. e) Coulometric curves for ORCF-3 V in 0.05 M $CuSO_4$ and 0.05 M K_2SO_4, respectively. f) Normalized, deconvoluted XPS $Cu2p_{3/2}$ spectra of UPD Cu-ORCF-3 V and $CuSO_4$-ORCF-3 V.

employ a combination of electrochemical techniques, X-ray photoelectron spectroscopy (XPS), and ex- and in situ X-ray absorption spectroscopy (XAS) to track the coordination environment of Cu atoms through the course of UPD. Finally, to showcase the performance of our transition metal SACs, we employ a Co-based SAC for electrochemical nitrate reduction to ammonia, a promising alternative to the energy-intensive Haber–Bosch process.

2. Results and Discussion

2.1. Functionalization of Oxidized Carbon Supports

Carbon-based electrode materials are favored in numerous applications owing to their tunable morphologies, good conductivity, and low costs. Accordingly, we selected reticulated carbon foam (RCF), a porous carbon electrode material with high

surface-area-to-volume ratio,[35] as model electrode material and SAC support. Prior to SAC synthesis, the RCF was modified via electrochemical oxidation to increase electrochemically active surface area (ECSA) and abundance of single-atom anchor-sites, such as oxygen-containing functional groups as well as lattice vacancies and defects.[36–38] Direct modification and use of RCF as base electrode and SAC support eliminates the need for attachment of catalyst/substrate via drop-casting or otherwise. The extent of oxidation was controlled by varying the applied potential from +1.0 to +4.0 V versus RHE.

Comparison of XPS C1s regions for pristine RCF and ORCF-x (oxidized RCF, where x represents oxidation potential) confirms successful functionalization of RCF with oxygen-containing moieties (Figure 1b) The peak distribution for pristine RCF resembles typical sp^2 carbon,[39] with a dominant C═C peak and small contributions from oxygen-containing moieties. Following oxidation, peaks corresponding to oxygen-functionalized carbon, particularly C—OH, O—C—O, and C═O moieties, become markedly more prominent. C/O ratios for each sample exhibit a similar trend, ranging from 12.1 in pristine RCF to 4.8 in ORCF-4 V (Figure 1c; and Table S1, Supporting Information).

In addition to oxygen-containing functional groups, we observed changes to both ECSA and carbon defect level in ORCF following oxidation. Double layer capacitance (DLC) measurements revealed a trend of dramatically increased ECSA with increasing oxidation potential (Figure 1d; and Figure S1, Supporting Information), illustrated by an ≈80-fold increase in ECSA of ORCF-4 V over pristine RCF. Interestingly, by comparison of D and G band intensities (i.e., $I_{D/G}$ ratio) in the Raman spectra of each sample (Figure S2, Supporting Information), we found no evidence of an increase in defect level following oxidation. In fact, due to the amorphous structure of reticulated carbon, pristine RCF demonstrates a relatively high $I_{D/G}$ ratio ratio of ≈1.15, which appears to decrease following the oxidation at potentials +3.0 V and greater. This may be due to excessive oxidation of the carbon support, which can result in evolution of CO_2(g) and delamination of defect-rich graphite layers.[40] Nevertheless, the higher Cu content of ORCF-3 V (now referred to as ORCF) following UPD (Figure 1c; and Note S1, Figures S3,S4, Table S2, Supporting Information) led us to select +3.0 V as the oxidation potential for subsequent investigation.

2.2. Synthesis and Characterization of Cu-ORCF SAC

As a starting point for developing a protocol for a more universal UPD synthesis strategy, we investigated UPD of Cu SACs on ORCF. Cu is well-suited for reductive electrochemical synthesis owing to its SRP of +0.34 V ($Cu^{2+} + 2e^- \rightarrow Cu^0$),[42] situated positive of the competing hydrogen evolution reaction (HER: $2H^+ + 2e^- \rightarrow H_{2\,(g)}$).[43] Moreover, unlike noble metals such as Pd and Pt, Cu^{2+} is readily soluble as a hydrated cation in neutral and acidic electrolytes,[44] avoiding the added complexity of ligands such as Cl^- and NH_3 in the deposition process.

Previous works investigating UPD for SAC synthesis employ cyclic voltammetry (CV) of the support material in precursor-containing electrolyte to select an appropriate potential for UPD (E_{UPD}) .[23,34] The success of this approach, however, depends on the homogeneity of the substrate surface, as well as its DLC, which may affect the sharpness and intensity of redox peaks above the background current.[45] Thus, heterogeneous substrate materials, possessing large ECSA and various single-atom anchor-sites, are unlikely to exhibit peaks corresponding to UPD phenomena.[27] In fact, a CV of ORCF in 0.05 M $CuSO_4$ (Figure S5, Supporting Information) shows no peaks attributable to Cu UPD. Rather, we postulate that by applying a constant potential close to but positive of a metal precursor's SRP (i.e., approaching its equilibrium potential), a high surface coverage of metal atoms can be achieved without formation of metal-metal bonds. To assess this hypothesis, we performed chronoamperometry (CA) on ORCF in Ar-saturated 0.05 M $CuSO_4$ at underpotentials of 200, 100, 50, and 25 mV relative to the Cu^{2+}/Cu^0 SRP, respectively (Figure S6, Supporting Information). The increase in magnitude of total charge passed as the deposition potential is shifted closer to the Cu^{2+}/Cu^0 SRP suggests an increase in extent of Cu UPD. Thus, to achieve a high loading of isolated Cu atoms on ORCF, while remaining safely positive of the Cu^{2+}/Cu^0 SRP, we selected an underpotential of 25 mV for further experiments.

To investigate the mechanism of Cu deposition, we performed CA experiments on ORCF working electrodes in blank (0.05 M K_2SO_4) and test (0.05 M $CuSO_4$) electrolytes. The resulting coulometric curves (Figure 1e) show that substantially more charge is passed in the presence of $CuSO_4$, suggesting that a reductive process involving Cu^{2+} has occurred. To further verify that Cu undergoes a Faradaic change during deposition (as opposed to physisorption alone), we performed XPS (Figure 1f) of UPD Cu-ORCF and ORCF with drop-casted $CuSO_4$ electrolyte (without any further treatment). The ≈2 eV shift of the primary Cu^{2+} peak toward lower binding energy in UPD Cu-ORCF is likewise suggestive of a change in chemical state following UPD.

We assessed atomic dispersion of Cu by evaluating the coordination environment of Cu-ORCF via XAS analysis. The Fourier transform (FT)-EXAFS region of Cu-ORCF (**Figure 2a**) contains a single peak at ≈1.6 Å, which aligns with the first shell Cu—O peak observed in CuO. The absence of any metal-metal peak, as observed at ≈2.3 Å in Cu foil, suggests that Cu sites in Cu-ORCF are atomically dispersed.[46] The Cu K-edge XANES (Figure 2b,c) shows an edge position and white-line intensity close to but higher than the CuO standard, suggesting an oxidation state slightly greater than +2.[47] This unusually high valence state of Cu_1 may result from the highly oxidized ORCF substrate, which provides an abundance of electron-withdrawing oxygen atoms that may coordinate with metal adatoms.[48] Note, however, that this high final oxidation state indicates that no net reduction occurs during the deposition of the precursor ion, which is initially in an oxidation state of +2. Thus, the UPD mechanism taken by Cu atoms in this work appears to differ from the more well-defined UPD of metals onto foreign metal substrates, in which the deposited metal tends to be reduced to a near-zero valent state.[28] Examination of the pre-edge features of UPD Cu-ORCF (Figure 2c) reveals a small peak at ≈8977 eV corresponding to dipole-forbidden 1s→3d transition, also indicative of Cu^{2+} species.[49] Interestingly, the *k*- and *R*- space fitting of Cu-ORCF FT-EXAFS (Figure 2d) yielded an average coordination number (CN) of 3.8 (Table S3, Supporting Information) despite the lack of a pre-edge peak at 8985 eV, which is typically present in tetra-coordinated Cu species.[50] However, the low intensity of the 1s→3d transition peak is more in-line with tetra-coordinated

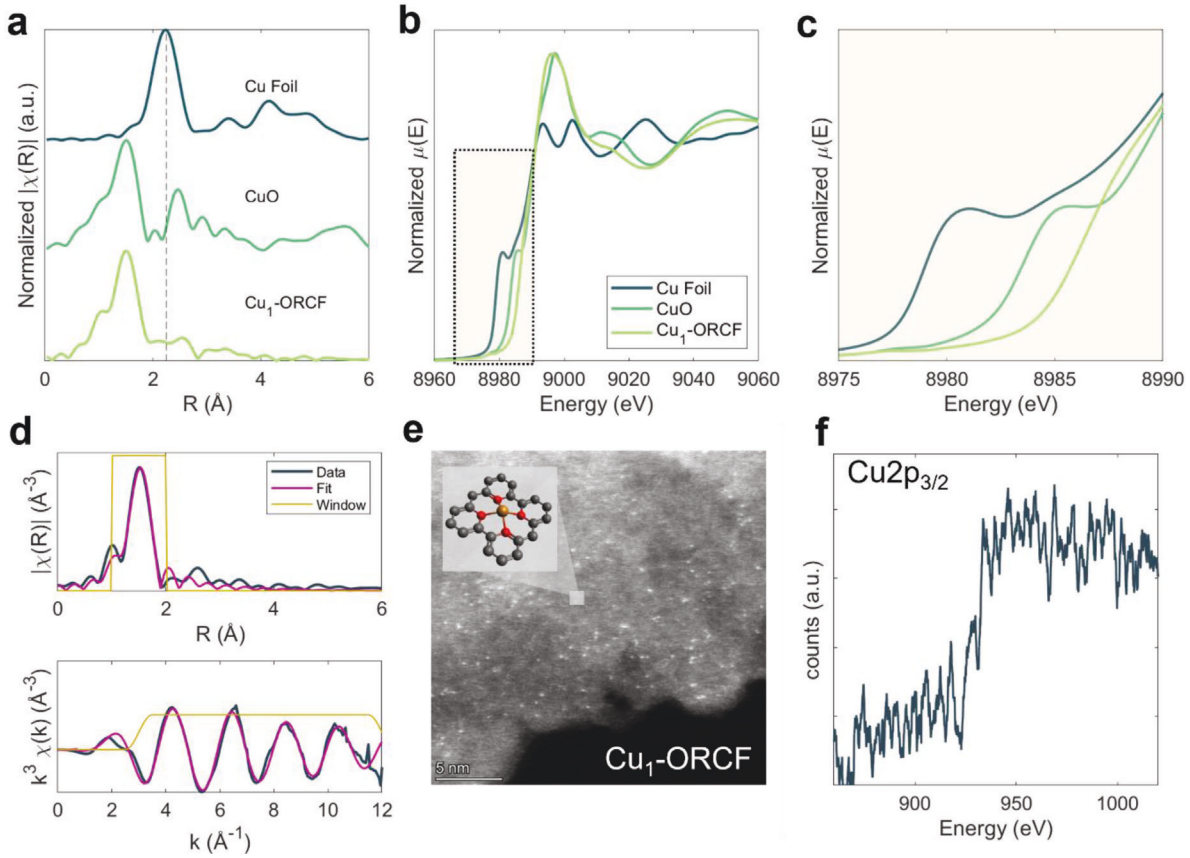

Figure 2. XAS and STEM characterization of Cu_1-ORCF. a) Comparison of FT-EXAFS. b) Full XANES region (shaded region represents approximately the axes limits of the pre-edge region enlarged in panel c). (c) and pre-edge only for Cu_1-ORCF and Cu standards. d) Fitted Cu K-edge FT-EXAFS (top) and EXAFS (bottom) of Cu_1-ORCF. e) Atomic-resolution HAADF-STEM image (scale bar is 5 nm) and graphical rendering of one plausible metal-site coordination structure of Cu_1-ORCF. f) $Cu2p_{3/2}$ regional EELS spectrum collected over a small region of Cu_1-ORCF containing multiple bright spots.

Cu species (e.g., CuO) than penta- or hexa-coordinated species (e.g., $Cu^{2+}_{(aq)}$).[51] This may suggest that Cu atoms in Cu_1-ORCF have a distorted square-planar or tetrahedral configuration (inset of Figure 2e).

Atomic-resolution images taken via high-angle annular dark field scanning transmission electron microscopy (HAADF-STEM) of Cu-ORCF depict isolated high-Z atoms dispersed across the sample surface, with no obvious signs of metallic clusters or nanoparticles (Figure 2e; and Figure S7, Supporting Information). Electron energy loss spectroscopy (EELS) of a limited region of the sample ($\approx 3 \times 3$ nm^2) containing multiple, dynamic atoms (Figure S8, Supporting Information) reveals an edge at ≈930 eV (Figure 2f; and Figure S9, Supporting Information), corresponding to the binding energy of the Cu $2p_{3/2}$ orbital. This confirms that the high-Z atoms observed in the HAADF-STEM images correspond to isolated Cu atoms on the ORCF substrate. The weight loading of Cu in Cu_1-ORCF was determined to be 0.36% ± 0.061% (Table S4, Supporting Information).

2.3. UPD Synthesis of Other 3D Transition Metal SACs

The data presented in the preceding sections provide strong evidence of successful synthesis of a Cu SAC supported on ORCF (now referred to as Cu_1-ORCF) by our UPD approach. Inspired by the rapid timescale and simplicity of UPD for Cu SAC synthesis, we sought to expand this approach to synthesize SACs consisting of Fe, Co, and Ni supported on ORCF. We hypothesized that it would be possible to obtain morphologically similar SACs by adjusting only the E_{UPD} and identity of metal precursor. For each metal, E_{UPD} was selected following the same rationale as described previously for Cu_1-ORCF. Table S5 (Supporting Information) summarizes the half-reaction, SRP, and selected E_{UPD} for each metal investigated. FT-EXAFS of Fe, Co, and Ni K-edge spectra confirms successful synthesis of Fe_1-ORCF, Co_1-ORCF, and Ni_1-ORCF, respectively (**Figure 3**a), evidenced by strong metal-oxide peaks and the absence of metal-metal peaks. As in the case of Cu_1-ORCF, Fe, Co, or Ni K-edge XANES of each respective material (Figures S10a,b, S11a,b, and S12a,b, Supporting Information) exhibit white-line intensities close to those of 2+ or 3+ metal oxide standards. The *k*- and *R*- space fitting of each catalyst yielded CNs of 3.6, 6.6, and 5.6 for Fe, Co, and Ni, respectively (Figures S10c,d, S11c,d, and S12c,d, Supporting Information), suggesting that Cu and Fe tend to form tetracoordinated configurations, while Co and Ni favor hexacoordinated octahedral configurations. This observation aligns well with the theory of crystal field stabilization energies for transition metal complexes; as $d^{[7]}$ and $d^{[8]}$ transition metals, respectively, Co and Ni tend to

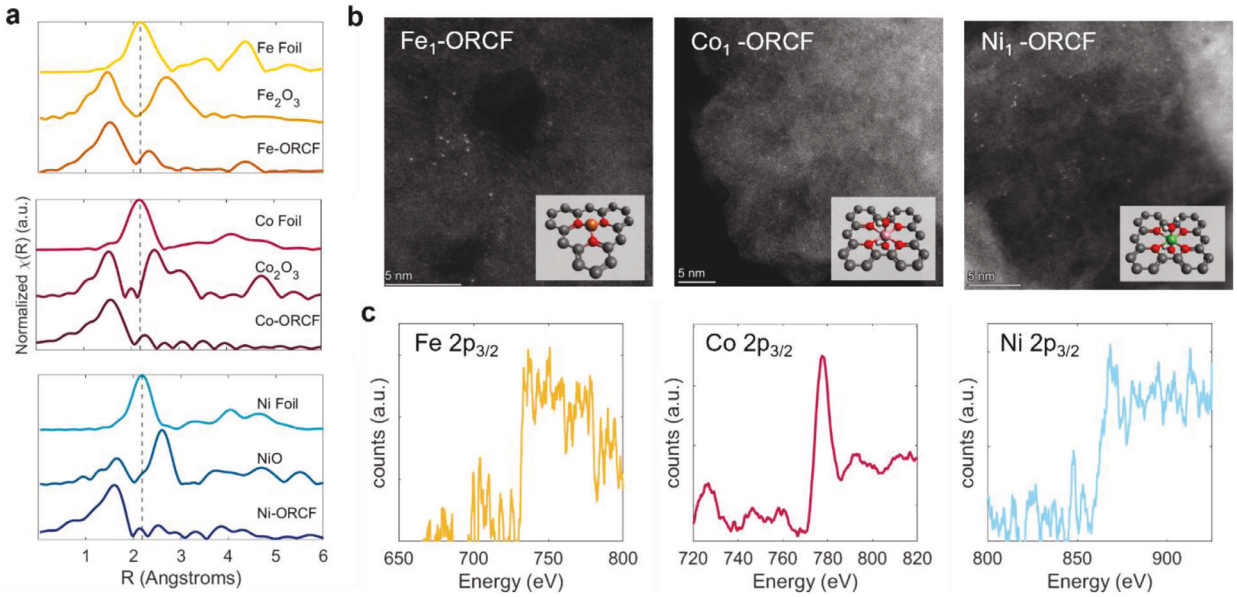

Figure 3. XAS and STEM/EELS characterization of additional monometallic transition metal SACs. a) Co, Fe, and Ni K-edge FT-EXAFS. b) HAADF-STEM images (scale bars = 5 nm) and graphical renderings of plausible metal-site coordination structures, and c) regional EELS spectra of Fe_1-ORCF, Co_1-ORCF, and Ni_1-ORCF, respectively.

have higher octahedral site preferences than Cu or Fe. Due to the strict geometric constraints of a saturated octahedral coordination sphere, however, it seems unlikely that all Co and Ni atoms in Co_1- and Ni_1-ORCF share bonds with only O-atoms of the substrate. We instead propose a hexacoordinated model in which each Co or Ni atom shares 4—6 bonds with O-containing groups of the substrate and 1—2 bonds to water ligands leftover from the precursor ion's coordination sphere (see insets of Figure 3b). We emphasize, however, that each of these modeled coordination environments present only one plausible configuration for the metal sites, while the highly disordered nature of oxidized carbon substrates implies that a variety of configurations may be possible. HAADF-STEM images of each metal show similar bright spots dispersed on ORCF, with no obvious signs of nanoparticles or metallic clusters (Figure 3b; and Figures S13–S15, Supporting Information). Scanning EELS was performed over small sections ($\approx 3 \times 3$ nm^2) of each sample (Figure 3c; and Figures S16–S18, Supporting Information) revealing edges corresponding to the $2p_{3/2}$ orbitals of each metal. Although the presence of hydrogen bubbles and activated hydrogen on the ORCF substrate may impact the overall efficiency of metal deposition, the cooccurrence of HER with UPD of Fe, Co, and Ni does not appear to affect the morphology of the resulting SAC.

2.4. UPD Synthesis of Bimetallic SACs

Bimetallic SACs present exciting opportunities for incorporating two distinct metal active sites into a single catalyst material.[52] The proximity of these atomically dispersed metal sites to one another has been shown to enable synergistic effects, resulting in improved catalytic performance over either metal alone.[53–55] For example, Fu et al., demonstrated improved performance of a bimetallic Ir-Mo SAC for selective reduction of 4-nitrostyrene (4-NS), owing to synergy between H_2 activating Ir_1 sites and preferential adsorption of 4-NS at Mo_1 sites.[54] Following successful synthesis of Cu_1-, Fe_1-, Co_1-, and Ni_1-ORCF catalysts, we sought to produce randomly interspersed bimetallic SACs by applying sequential UPD steps in separate electrolytes. Following this strategy, we synthesized FeCu-, CoCu-, and NiCu-ORCF SACs by depositing Fe, Co, or Ni onto freshly synthesized Cu_1-ORCF. In each case, Cu was deposited first because of its positive reduction potential compared to the other metals (Table S5, Supporting Information), which prevents galvanic displacement of Cu atoms by less-noble Fe, Co, or Ni ions during the second UPD step.[23] Cu, Fe, Co, and Ni K-edge FT-EXAFS and XANES for FeCu-ORCF, CoCu-ORCF, and NiCu-ORCF resemble those of respective monometallic counterparts (**Figure** 4a; and Figures S19–S21, Supporting Information). In addition to metal-oxide peaks and absence of metallic bonding, the spectra show no evidence of bonding between the two metals deposited (i.e., alloying) nor any other noticeable influences of Fe, Co, or Ni on the Cu coordination environment. HAADF-STEM images (Figure 4b; and Figures S22–S24, Supporting Information) of FeCu-ORCF, CoCu-ORCF, and NiCu-ORCF depict similar high-Z atoms dispersed on ORCF supports. EELS spectra (Figure 4c,d; and Figures S25–S27, Supporting Information) exhibit edges for both atomic species in each bimetallic sample, suggesting that the dispersed single-atoms are a mixture of the two deposited metals. Identities of individual metal atoms were not distinguishable via EELS due to low signal intensity at subatomic resolution and movement of metal atoms under the incident electron beam.[56]

2.5. UPD of Cu on Additional Oxidized Carbon Substrates

Although useful for fundamental investigations into UPD-based SAC synthesis, the poor mechanical stability and high cost of RCF limits its feasibility in practical applications. We therefore

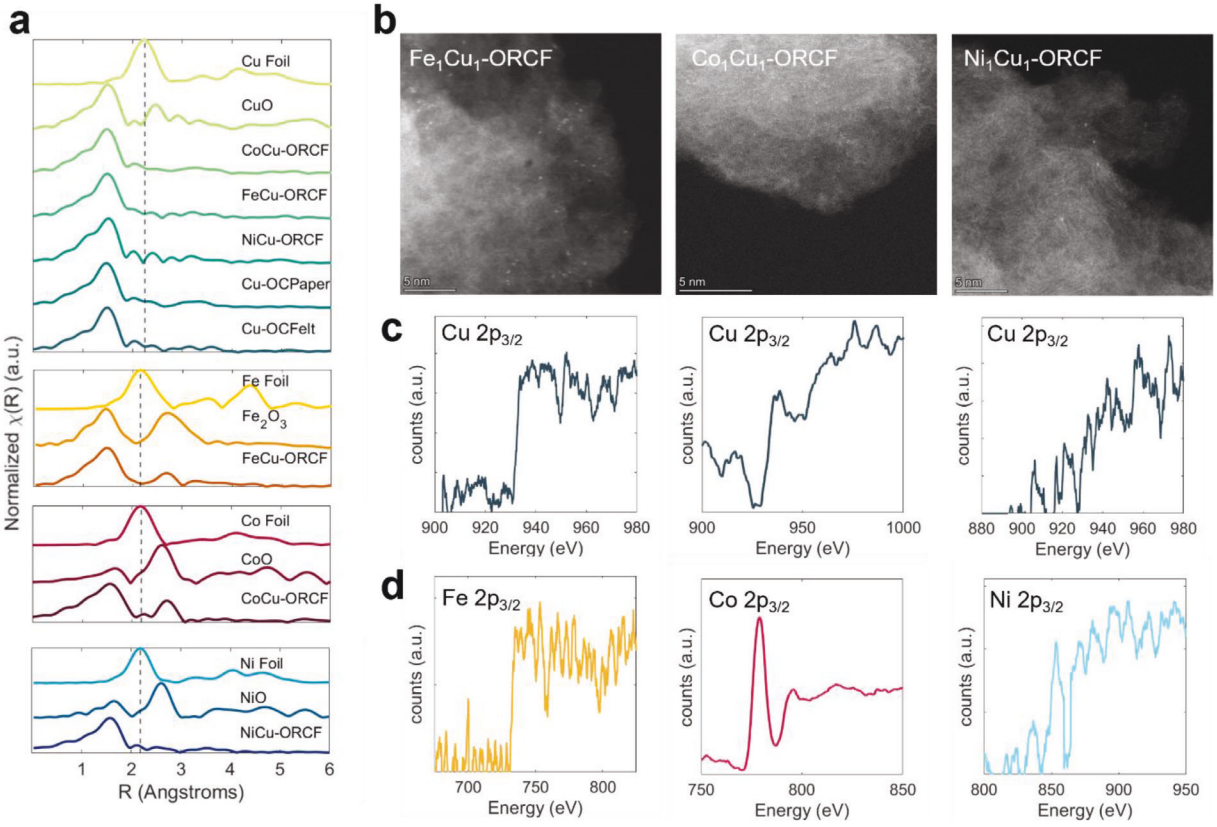

Figure 4. XAS and STEM/EELS characterization of bimetallic SACs and Cu SACs on additional substrates. a) FT-EXAFS of Cu, Fe, Co, and Ni K-edges for respective Cu and bimetallic SACs. b) HAADF-STEM images (scale bars = 5 nm), c) Cu $2p_{3/2}$ EELS edges, and d) Fe, Ni, and Co $2p_{3/2}$ EELS edges of Fe_1Cu_1-, Co_1Cu_1-, and Ni_1Cu_1-ORCF, respectively.

applied our synthesis methodology to two additional commonly employed electrode materials, Sigracet carbon paper and carbon felt. Sigracet carbon paper is a robust, highly porous electrode material consisting of interwoven carbon fibers coated with a carbon black microporous layer, ideal for use in gas diffusion cells.[57–59] Carbon felt consists of thread-like fibers of carbon which form a soft, flexible network of pores. It is typically less dense and more hydrophilic than carbon paper and is well-suited for flow-through applications.[60] Prior to UPD, each material was similarly oxidized at +3.0 V to introduce oxygen-containing functional groups and increase ECSA. XPS C1s spectra of the oxidized materials (denoted OCPaper and OCFelt, Figures S28,S29, Supporting Information) show an abundance of oxygen-containing functional groups. Cu UPD was performed on each material at an underpotential of 25 mV (vs Cu^{2+}/Cu^0 SRP) to produce Cu-OCPaper and Cu-OCFelt. FT-EXAFS (Figure 4a; and Figures S30,S31, Supporting Information) and HAADF-STEM images (Figures S32,S33) of Cu-OCPaper and Cu-OCFelt confirmed atomic dispersion of Cu in each material. These results underscore the versatility of UPD to produce SACs supported on a range of commercial carbon-based electrode materials.

2.6. In Situ XAS of Cu UPD

Although ex situ characterization as discussed above can confirm formation of atomically dispersed metal-substrate bonds following UPD, it provides little information on the metal's coordination environment during UPD. Thus, we performed in-situ XAS to track transformation of Cu atoms from aqueous ions to oxygen-coordinated single-atoms under UPD conditions (see the Experimental Section for experimental details). At open circuit potential (OCP), prior to application of E_{UPD}, a strong background signal corresponding to hydrated Cu^{2+} (**Figure 5a**) near the electrode was observed and remained unchanged over a 5 min period. Following application of E_{UPD}, we observed slight changes in the total signal, including reduction in white-line intensity and growth of a small pre-edge peak at 8980 eV, which we attribute to formation of Cu_1 bonds with surface-bound oxygen groups on the electrode.

Subtraction of the background Cu^{2+} signal collected at OCP enabled us to isolate the component spectra of this newly formed species (Figure 5a), which appeared following the first scan at E_{UPD} and continued to grow in intensity throughout the 10 min experiment (Figure 5b). Analysis of the total spectra via singular value decomposition confirmed that only two spectral components were present throughout the experiment (Figure 5c; and Note S2, Supporting Information). Fitting the spectral series with the extracted spectra of newly formed species and the hydrated Cu^{2+} allowed us to estimate their relative concentrations (Figure 5d). Interestingly, the spectrum of Cu_1 formed in situ (Cu_1-in situ) differs from that of Cu_1-ex situ, obtained after air-drying of the electrode. While Cu_1-ex situ exhibits mostly Cu^{2+} character, Cu_1-in situ possesses notably more Cu^+ character,

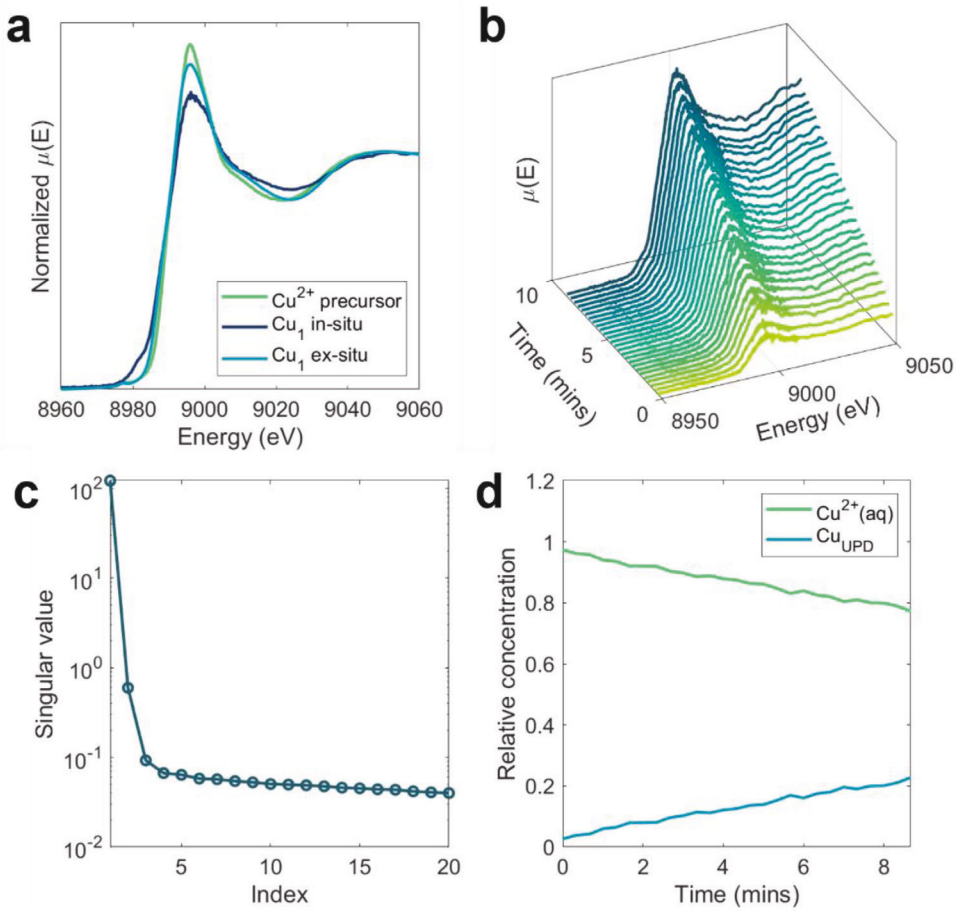

Figure 5. In situ XAS and singular value decomposition of an oxidized carbon paper electrode during Cu UPD. a) Cu K-edge XANES of the electrode in Cu electrolyte, but prior to application of potential (adsorbed/dissolved Cu^{2+} precursor only), under the applied UPD potential (in situ), and in air after drying (ex situ). b) Non-normalized, background subtracted Cu K-edge XANES of the oxidized carbon paper electrode during UPD. c) Singular values of the first 20 computed spectral components. d) Relative concentrations of Cu^{2+}(aq) and the underpotentially deposited Cu_1 species.

evidenced by its diminished white-line intensity and pre-edge peak ≈8980 eV.[61] This suggests that UPD may proceed via reduction of $Cu^{2+}_{(aq)}$ to a partially reduced intermediate Cu—O species which, upon air-exposure, reconfigures to an oxidation state of ≈+2. In addition to providing insight on the timescale of SAC formation via UPD, this finding may underscore the importance of electron-rich anchor-sites (e.g., oxygen atoms) in facilitating reduction of $Cu^{2+}_{(aq)}$ to form stable metal-substrate bonds during UPD.

2.7. Electrochemical Nitrate Reduction to Ammonia

SACs have demonstrated excellent performance for selective reduction of nitrate to ammonia, often displaying higher NH_3 Faradaic efficiency (FE) and intrinsic activity compared to nanostructured counterparts.[61–64] Cu is typically considered the benchmark catalyst for electrochemical nitrate reduction to ammonia (NO_3R), owing to its high activity for the rate limiting step of NO_3^- to NO_2^- and its relatively weak interaction with hydrogen, which inhibits the competing HER reaction.[63,65] However, recent studies have reported exceptional performance of Co-based catalysts attributed to formation of active hydrogen on Co active-sites, which boosts ammonia selectivity by mediating the efficient transfer of H-atoms to the central N-atom of intermediate species.[64,66] Inspired by these findings, we selected Co_1-OCPaper as a model NO_3R catalyst to showcase the performance of our UPD-synthesized SACs.

As an initial screening of the catalytic performance of Co_1-OCPaper for NO_3R, linear sweep voltammetry (LSV) was performed in Ar-saturated electrolytes containing nitrate (0.1 M KNO_3 + 0.1 M K_2SO_4, pH 11.5) and supporting electrolyte only (0.1 M K_2SO_4, pH 11.5, **Figure 6**a). The dramatic increase in current density in the presence of KNO_3, starting at an onset potential of −0.1 V, suggests high selectivity of Co_1-OCPaper for reduction of NO_3^- over background HER. Electrocatalytic performance was further assessed via 1 h batch experiments at fixed potentials from −0.2 to −0.8 V in 0.1 M KNO_3 + 0.1 M K_2SO_4 (Figure 6b), following which NH_3 and NO_2^- products were quantified using UV–vis spectrophotometry (see the Experimental Section; and Figures S34,S35, Supporting Information). The results show a steady increase in NH_3 yield rate, from 280 μg h^{-1} cm^{-2} at −0.2 V to 3900 μg h^{-1} cm^{-2} at −0.8 V, as the potential is shifted to more negative values. Meanwhile, NH_3 selectivity (herein used

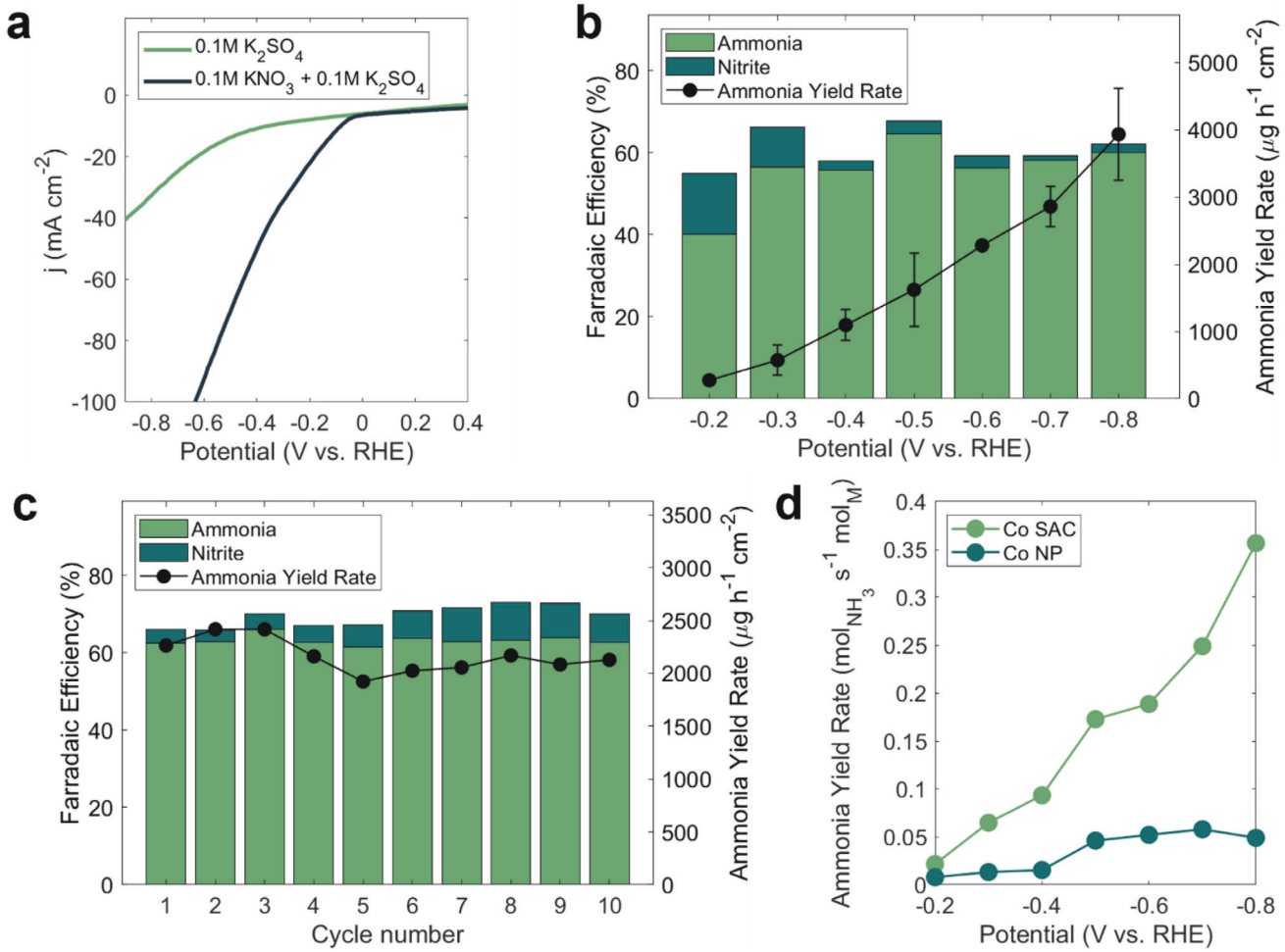

Figure 6. Electrochemical NO_3RR performance of Co_1-OCPaper. a) LSVs of Co_1-ORCF in 0.1 M K_2SO_4 and 0.1 M KNO_3 + 0.1 M K_2SO_4, respectively. b) NH_3 and NO_2^- FE and NH_3 yield rate in 0.1 M KNO_3 + 0.1 M K_2SO_4, measured following 1 h batch experiments at a range of potentials. c) Performance of Co_1-OCPaper in 0.1 M KNO_3 + 0.1 M K_2SO_4 over the course of 10 1 h cycles at −0.5 V. d) Metal content-normalized ammonia yield rates of Co_1-OCPaper and Co_{NP}-OCPaper.

interchangeably with FE) rose from 40% at −0.2 V to 64% at −0.5 V, remaining consistently >55% for all potentials −0.3 V and more negative. Production of NO_2^- remained low (1–10% of total FE) across all potentials (Figure 6b). Based on previous literature elucidating the critical role of H* in facilitating the reduction of NO_3^- to NH_3 over Co-based catalysts,[66,67] we attribute the strong catalytic performance of Co_1-OCPaper to the controlled production of H* by Co active sites and their ability to rapidly transfer H* to NO_3^-.

Co_1-OCPaper demonstrated reasonable stability over 10, 1 h cycles at −0.5 V (Figure 6c), sustaining an NH_3 selectivity of >60% and yield rate of ≈1500 μg h^{-1} cm^{-2}. No major differences were observed in FT-EXAFS of Co_1-OCPaper before and after the repeated cycling (Figure S36, Supporting Information). Figure 6d contrasts the NO_3R performance of Co_1-OCPaper with that of a Co-nanoparticle catalyst supported on OCPaper (Co_{NP}-OCPaper, characterization in Figures S37,S38, Supporting Information). The larger Co-mass-normalized NH_3 yield rate of Co_1-OCPaper across the entire potential range reflects the higher intrinsic activity of Co single-atom sites compared to Co_{NP}-OCPaper, and is in accordance with previous studies comparing the performance of Fe-, Cu-, Co-, and Ru-based SACs to benchmark nanoparticle catalysts.[62–64] These findings exemplify the catalytic performance of our UPD-synthesized SACs for a relevant electrochemical application.

3. Conclusions

Application of UPD toward SAC synthesis has been confined almost exclusively to Cu-based catalysts on a narrow range of support materials, likely due to the analytical challenges posed by substrate heterogeneity and co-occurrence of HER, which make it difficult to identify suitable E_{UPD}. In this work, by selecting E_{UPD} based solely on a metal's SRP, we demonstrated for the first time that UPD can be adapted to synthesize oxygen-bound SACs of 3d transition metals less-noble than Cu. In addition, we showed that UPD can be applied sequentially to obtain bimetallic SACs and performed directly onto commercial electrode materials, eliminating the need for inks or binders. These findings expand upon the usefulness and versatility of UPD for SAC synthesis, with

hopes of enabling future research toward realization of fast, reliable, and fully electrified SAC synthesis processes.

4. Experimental Section

Materials: All chemical reagents were purchased from Sigma-Aldrich (Missouri, USA) and were of ACS Reagent grade or higher. Reticulated carbon foam was purchased from Goodfellow Corporation (Pennsylvania, USA). Carbon paper (Sigracet 39BB) and carbon felt (AvCarb 100) were purchased from Fuel Cell Store (Colorado, USA).

Preparation of Oxidized Carbon Substrates: Oxidized carbon substrates were prepared by electrochemical oxidation in an undivided, 3-electrode glass cell. A carbon rod (99.95% purity, Fischer) and Ag/AgCl electrode (sat. KCl, CH Instruments) were used as the counter and reference electrodes, respectively. In a typical procedure, 1 cm^2 of carbon-material working electrode (2 × 0.5 cm^2) was submerged in 0.1 M H_2SO_4 and connected to a VSP-128 electrochemical workstation (Biologic, USA) using alligator clips. A fixed oxidative potential (+1.0 to +4.0 V) was applied for 300 s, after which the working electrode was removed and rinsed thoroughly with deionized water (18.2 MΩ).

UPD Synthesis of Cu SACs: UPD experiments were performed in an undivided glass cell identical to that used for substrate oxidation. In a typical experiment 1 cm^2 of oxidized carbon working electrode (2 cm^2 total area) was submerged in Ar-saturated electrolyte containing 0.05 M $CuSO_4$ and 5 mM H_2SO_4. The system was left at open circuit potential (OCP) for 5 min prior to deposition to allow time for sorption of metal ions to take place on the electrode surface. Then, an underpotential of +25 mV (vs Cu^{2+}/Cu^0 SRP) was applied to the working electrode for a duration of 300 s. The as-obtained SAC electrode was removed from electrolyte and rinsed thoroughly with deionized water.

UPD Synthesis of Other Transition Metal SACs: Fe, Co, and Ni SACs were synthesized following a similar procedure as in the case of Cu. In each case, an underpotential of +25 mV versus the respective metal's SRP was applied for 300 s. Analogous electrolyte compositions were employed for each synthesis, namely combinations of 5 mM H_2SO_4 with 0.05 M $FeSO_4$, $CoCl_2$, or $NiNO_3$, respectively, to yield a 0.05 M solution of hydrated metal cation. Bimetallic SACs consisting of FeCu, CoCu, and NiCu, were obtained by depositing each metal in sequence, starting with the nobler metal (Cu) to avoid galvanic displacement.

Electrochemical Synthesis of Co_{NP}-OCPaper: Co_{NP}-OCPaper was prepared by reductive electrodeposition of Co onto as-prepared OCPaper substrate (oxidized at 3.0 V for 300 s). Reaction conditions were kept identical to those used for synthesis of Co SACs, except that an overpotential of 0.5 V (vs Co^{2+}/Co^0 SRP) was applied to induce formation of Co—Co bonds.

HAADF-STEM/EELS Imaging and Analysis: Aberration corrected HAADF-STEM images and EELS spectra were obtained using an aberration corrected Titan Themis AC-STEM (ThermoFisher Scientific, USA) equipped with a Gatan Quanta GIF spectrometer (AMETEC, Inc., USA) at the Thermo Fisher Scientific Center for Advanced Microscopy and Materials Analysis at UConn. The Themis was operated at 300 keV with a beam current of ≈0.285 nA (spot size: 5, CLA aperture: 70 µm) for imaging and electron energy loss spectroscopy (EELS). Imaging was done using 130 mm camera length and the HAADF detector. For EELS, the 5 mm GIF aperture was used with a camera length of 21 mm ("Filtered" off, and "Descan" on) and a GIF dispersion of 0.1 or 0.25 eV per channel, depending on the sample. The GIF energy window was varied for each metal sample to contain the respective metal peak of interest and a sufficient pre-peak region for background subtraction. EELS spectra acquisition was done, while the STEM beam was scanning over an ≈3 nm × 3 nm square on the sample that contained metal atoms, and thus EELS spectra contained signal from all the single atoms within the scanning region.

XAS Measurements and Data Analysis: XAS measurements were collected at Beamline 8-ID (ISS) of the National Synchrotron Light Source II located at Brookhaven National Laboratory, USA. The synchrotron's storage ring was operating at 3 GeV with a beam current of 400.1 mA. Measurements of Cu, Fe, Co, and Ni k-edges were acquired in fluorescence mode using a Si(111) double crystal monochromator and a passivated implanted planar silicon fluorescence detector at room temperature. For ex situ measurements, samples were prepared either by grinding and casting as pellets using poly(ethylene glycol) as a binder (carbon foam, felt substrates) or by cutting and stacking of as-obtained electrodes (carbon paper substrates). All samples were placed into 12 mm sample holders and sealed with Kapton film. In situ XAS experiments were performed under the same synthesis conditions as used in the preparation of ex situ samples, except that a custom 3D-printed cell with 1 cm diameter Kapton tape window was used in place of a typical glass H-cell. All in situ experiments were performed at room temperature with OCPaper as working electrode, plain carbon paper (Sigracet 39BB) as counter, and Ag/AgCl (sat. KCl) as reference. Collected spectra were processed and analyzed using Athena and Artemis software packages, including conversion of raw data to µ(E), background subtraction, normalization, Fourier Transform, and mathematical fittings.

Additional Materials Characterization: XPS data were collected using a monochromatic 1486.7 eV Al Kα X-ray source on PHI VersaProbe II X-ray Photoelectron Spectrometer (Physical Electronics, USA). Raman spectroscopy was performed via Horiba LabRAM HR Evolution Raman spectrometer (Horiba Instruments, Japan). ICP-MS was performed using a Perkin Elmer ICP-MS Elan DRC-e (PerkinElmer, USA).

Electrochemical Nitrate Reduction Experiments: Nitrate reduction experiments were performed in batch mode in a standard 2-compartment H-cell divided by a Nafion 117 cation exchange membrane (Fuel Cell Store, USA). Ag/AgCl (sat. KCl) and platinized Ti-mesh electrodes were used as reference and counter, respectively. An electrolyte consisting of 0.1 M KNO_3 + 0.1 M K_2SO_4 was used as the test electrolyte, unless otherwise specified. Prior to use, electrolyte pH was adjusted to 11.5 by dropwise addition of 1 M KOH solution to preempt the rapid change in pH caused by the consumption of H^+ during NO_3RR. The cell was continuously sparged with high-purity Ar gas (99.995%) and left to equilibrate for 15 min prior to the application of potential. A fixed potential was then applied to the working electrode for a duration of 1 h under vigorous stirring (600 rpm) and continuous sparging with Ar.

Quantification of Nitrate Reduction Products: Quantification of ammonia and nitrite as performed via spectrophotometry using modified forms of the indophenol blue (ammonia) and Greiss (nitrite) methods, as reported in the work of Wu et al.[62]

Supporting Information

Supporting Information is available from the Wiley Online Library or from the author.

Conflict of Interest

The authors declare no conflict of interest.

Data Availability Statement

The data that support the findings of this study are available on request from the corresponding author. The data are not publicly available due to privacy or ethical restrictions.

Keywords

electrochemical, nitrate reduction, single atom catalyst, synthesis, underpotential deposition

Received: October 28, 2023
Revised: January 26, 2024
Published online:

[1] S. Weon, D. Huang, K. Rigby, C. Chu, X. Wu, J.-H. Kim, *ACS ES&T Engg.* **2021**, *1*, 157.
[2] S. Ding, M. J. Hülsey, J. Pérez-Ramírez, N. Yan, *Joule* **2019**, *3*, 2897.
[3] S. K. Kaiser, Z. Chen, D. Faust Akl, S. Mitchell, J. Pérez-Ramírez, *Chem. Rev.* **2020**, *120*, 11703.
[4] R. Lang, X. Du, Y. Huang, X. Jiang, Q. Zhang, Y. Guo, K. Liu, B. Qiao, A. Wang, T. Zhang, *Chem. Rev.* **2020**, *120*, 11986.
[5] A. Wang, J. Li, T. Zhang, *Nat. Rev. Chem.* **2018**, *2*, 65.
[6] Q. Zhang, J. Guan, *Adv. Funct. Mater.* **2020**, *30*, 2000768.
[7] R. Qin, P. Liu, G. Fu, N. Zheng, *Small Methods* **2018**, *2*, 1700286.
[8] J. Wu, L. Xiong, B. Zhao, M. Liu, L. Huang, *Small Methods* **2020**, *4*, 1900540.
[9] X. Hai, S. Xi, S. Mitchell, K. Harrath, H. Xu, D. F. Akl, D. Kong, J. Li, Z. Li, T. Sun, H. Yang, Y. Cui, C. Su, X. Zhao, J. Li, J. Pérez-Ramírez, J. Lu, *Nat. Nanotechnol.* **2022**, *17*, 174.
[10] S. Zhao, G. Chen, G. Zhou, L. C. Yin, J. P. Veder, B. Johannessen, M. Saunders, S. Z. Yang, R. De Marco, C. Liu, *Adv. Funct. Mater.* **2020**, *30*, 1906157.
[11] Y. Yao, Z. Huang, P. Xie, L. Wu, L. Ma, T. Li, Z. Pang, M. Jiao, Z. Liang, J. Gao, Y. He, D. J. Kline, M. R. Zachariah, C. Wang, J. Lu, T. Wu, T. Li, C. Wang, R. Shahbazian-Yassar, L. Hu, *Nat. Nanotechnol.* **2019**, *14*, 851.
[12] P. Baldaguez Medina, S. Cotty, K. Kim, J. Elbert, X. Su, *Environ. Sci.: Water Res. Technol.* **2021**, *7*, 2231.
[13] X. He, Q. He, Y. Deng, M. Peng, H. Chen, Y. Zhang, S. Yao, M. Zhang, D. Xiao, D. Ma, B. Ge, H. Ji, *Nat. Commun.* **2019**, *10*, 3663.
[14] H. Yang, L. Shang, Q. Zhang, R. Shi, G. I. N. Waterhouse, L. Gu, T. Zhang, *Nat. Commun.* **2019**, *10*, 4585.
[15] J. Fonseca, J. Lu, *ACS Catal.* **2021**, *11*, 7018.
[16] C. Wang, X.-K. Gu, H. Yan, Y. Lin, J. Li, D. Liu, W.-X. Li, J. Lu, *ACS Catal.* **2017**, *7*, 887.
[17] N. Cheng, S. Stambula, D. Wang, M. N. Banis, J. Liu, A. Riese, B. Xiao, R. Li, T.-K. Sham, L.-M. Liu, G. A. Botton, X. Sun, *Nat. Commun.* **2016**, *7*, 13638.
[18] L. Han, H. Cheng, W. Liu, H. Li, P. Ou, R. Lin, H.-T. Wang, C.-W. Pao, A. R. Head, C.-H. Wang, X. Tong, C.-J. Sun, W.-F. Pong, J. Luo, J.-C. Zheng, H. L. Xin, *Nat. Mater.* **2022**, *21*, 681.
[19] W. Zhou, Z. Jiang, M. Chen, Z. Li, X. Luo, M. Guo, Y. Yang, T. Yu, C. Yuan, S. Wang, *Chem. Eng. J.* **2022**, *428*, 131210.
[20] Z. Lu, M. Piernavieja-Hermida, C. H. Turner, Z. Wu, Y. Lei, *J. Phys. Chem. C* **2018**, *122*, 1688.
[21] H. Yan, X. Zhao, N. Guo, Z. Lyu, Y. Du, S. Xi, R. Guo, C. Chen, Z. Chen, W. Liu, *Nat. Commun.* **2018**, *9*, 3197.
[22] Z. Zhang, C. Feng, C. Liu, M. Zuo, L. Qin, X. Yan, Y. Xing, H. Li, R. Si, S. Zhou, J. Zeng, *Nat. Commun.* **2020**, *11*, 1215.
[23] Y. Shi, W.-M. Huang, J. Li, Y. Zhou, Z.-Q. Li, Y.-C. Yin, X.-H. Xia, *Nat. Commun.* **2020**, *11*, 4558.
[24] J.-C. Liu, H. Xiao, J. Li, *J. Am. Chem. Soc.* **2020**, *142*, 3375.
[25] M. Zhou, J. E. Dick, A. J. Bard, *J. Am. Chem. Soc.* **2017**, *139*, 17677.
[26] H. E. M. Hussein, R. J. Maurer, H. Amari, J. J. P. Peters, L. Meng, R. Beanland, M. E. Newton, J. V. Macpherson, *ACS Nano* **2018**, *12*, 7388.
[27] O. A. Oviedo, L. Reinaudi, S. G. García, E. P. M. Leiva, *Monographs in Electrochemistry*, Springer, Cham **2016**, pp. 1–15.
[28] S. Szabó, *Int. Rev. Phys. Chem.* **1991**, *10*, 207.
[29] J. Orozco, C. Fernández-Sánchez, C. Jiménez-Jorquera, *Environ. Sci. Technol.* **2008**, *42*, 4877.
[30] A. Bewick, J. Jovićević, B. Thomas, *Faraday Symp. Chem. Soc.* **1977**, *12*, 24.
[31] H. Oh, Y. Park, H. Song, *J. Phys. Chem. C* **2020**, *124*, 20398.
[32] J. Kester, *J. Chem. Phys.* **1983**, *78*, 7466.
[33] A. Martínez-Ruíz, M. Palomar-Pardavé, J. Valenzuela-Benavides, M. H. Farías, N. Batina, *J. Phys. Chem. B* **2003**, *107*, 11660.
[34] J. Xu, R. Li, C.-Q. Xu, R. Zeng, Z. Jiang, B. Mei, J. Li, D. Meng, J. Chen, *Appl. Catal., B* **2021**, *289*, 120028.
[35] J. M. Friedrich, C. Ponce-de-León, G. W. Reade, F. C. Walsh, *J. Electroanal. Chem.* **2004**, *561*, 203.
[36] X. Ge, G. Su, W. Che, J. Yang, X. Zhou, Z. Wang, Y. Qu, T. Yao, W. Liu, Y. Wu, *ACS Catal.* **2020**, *10*, 10468.
[37] M. D. Hossain, Z. Liu, M. Zhuang, X. Yan, G. L. Xu, C. A. Gadre, A. Tyagi, I. H. Abidi, C. J. Sun, H. Wong, *Adv. Energy Mater.* **2019**, *9*, 1803689.
[38] M. M. Saleh, M. I. Awad, T. Okajima, K. Suga, T. Ohsaka, *Electrochim. Acta* **2007**, *52*, 3095.
[39] W. Xie, L.-T. Weng, K. M. Ng, C. K. Chan, C.-M. Chan, *Carbon* **2015**, *94*, 740.
[40] P. Feicht, R. Siegel, H. Thurn, J. W. Neubauer, M. Seuss, T. Szabó, A. V. Talyzin, C. E. Halbig, S. Eigler, D. A. Kunz, A. Fery, G. Papastavrou, J. Senker, J. Breu, *Carbon* **2017**, *114*, 700.
[41] M. C. Biesinger, *Appl. Surf. Sci.* **2022**, *597*, 153681.
[42] A. J. Bard, R. Parsons, J. Jordan, *Standard Potentials in Aqueous Solution*, Taylor & Francis, New York, **1985**.
[43] Y. Yi, G. Weinberg, M. Prenzel, M. Greiner, S. Heumann, S. Becker, R. Schlögl, *Catal. Today* **2017**, *295*, 32.
[44] K. S. Egorova, V. P. Ananikov, *Angew. Chem., Int. Ed.* **2016**, *55*, 12150.
[45] A. J. Bard, L. R. Faulkner, H. S. White, *Electrochemical Methods: Fundamentals and Applications*, John Wiley & Sons, New York **2022**.
[46] W. Zang, T. Yang, H. Zou, S. Xi, H. Zhang, X. Liu, Z. Kou, Y. Du, Y. P. Feng, L. Shen, L. Duan, J. Wang, S. J. Pennycook, *ACS Catal.* **2019**, *9*, 10166.
[47] K. Zhao, X. Nie, H. Wang, S. Chen, X. Quan, H. Yu, W. Choi, G. Zhang, B. Kim, J. G. Chen, *Nat. Commun.* **2020**, *11*, 2455.
[48] Y. Li, Z.-S. Wu, P. Lu, X. Wang, W. Liu, Z. Liu, J. Ma, W. Ren, Z. Jiang, X. Bao, *Adv. Sci.* **2020**, *7*, 1903089.
[49] J. Rudolph, C. R. Jacob, *Inorg. Chem.* **2018**, *57*, 10591.
[50] A. A. Guda, S. A. Guda, A. Martini, A. N. Kravtsova, A. Algasov, A. Bugaev, S. P. Kubrin, L. V. Guda, P. Šot, J. A. van Bokhoven, C. Copéret, A. V. Soldatov, *npj Comput. Mater.* **2021**, *7*, 203.
[51] A. Gaur, B. D. Shrivastava, K. Srivastava, J. Prasad, *X-Ray Spectrom.* **2014**, *43*, 238.
[52] M. Fan, J. Cui, J. Wu, R. Vajtai, D. Sun, P. M. Ajayan, *Small* **2020**, *16*, 1906782.
[53] S. K. Kaiser, A. H. Clark, L. Cartocci, F. Krumeich, J. Pérez-Ramírez, *Small* **2021**, *17*, 2004599.
[54] J. Fu, J. Dong, R. Si, K. Sun, J. Zhang, M. Li, N. Yu, B. Zhang, M. G. Humphrey, Q. Fu, J. Huang, *ACS Catal.* **2021**, *11*, 1952.
[55] M.-J. Cheng, E. L. Clark, H. H. Pham, A. T. Bell, M. Head-Gordon, *ACS Catal.* **2016**, *6*, 7769.
[56] A. Suzuta, K. Yamazaki, K. Gohara, T. Uchida, *J. Phys. Chem. C* **2022**, *126*, 12780.
[57] A. B. Moss, S. Garg, M. Mirolo, C. A. Giron Rodriguez, R. Ilvonen, I. Chorkendorff, J. Drnec, B. Seger, *Joule* **2023**, *7*, 350.
[58] J. Lim, S. Y. Choi, J. W. Lee, S. Y. Lee, H. Lee, *Proc. Natl. Acad. Sci. USA* **2023**, *120*, 2221438120.
[59] S. Overa, B. S. Crandall, B. Shrimant, D. Tian, B. H. Ko, H. Shin, C. Bae, F. Jiao, *Nat. Catal.* **2022**, *5*, 738.
[60] T. X. H. Le Huong, M. Bechelany, M. Cretin, *Carbon* **2017**, *122*, 564.
[61] J. Yang, H. Qi, A. Li, X. Liu, X. Yang, S. Zhang, Q. Zhao, Q. Jiang, Y. Su, L. Zhang, J.-F. Li, Z.-Q. Tian, W. Liu, A. Wang, T. Zhang, *J. Am. Chem. Soc.* **2022**, *144*, 12062.
[62] Z.-Y. Wu, M. Karamad, X. Yong, Q. Huang, D. A. Cullen, P. Zhu, C. Xia, Q. Xiao, M. Shakouri, F.-Y. Chen, J. Y. Kim, Y. Xia, K. Heck, Y. Hu, M. S. Wong, Q. Li, I. Gates, S. Siahrostami, H. Wang, *Nat. Commun.* **2021**, *12*, 2870.
[63] T. Zhu, Q. Chen, P. Liao, W. Duan, S. Liang, Z. Yan, C. Feng, *Small* **2020**, *16*, 2004526.

[64] J. Li, M. Li, N. An, S. Zhang, Q. Song, Y. Yang, J. Li, X. Liu, *Proc. Natl. Acad. Sci. USA* **2022**, *119*, 2123450119.
[65] G.-F. Chen, Y. Yuan, H. Jiang, S.-Y. Ren, L.-X. Ding, L. Ma, T. Wu, J. Lu, H. Wang, *Nat. Energy* **2020**, *5*, 605.
[66] K. Fan, W. Xie, J. Li, Y. Sun, P. Xu, Y. Tang, Z. Li, M. Shao, *Nat. Commun.* **2022**, *13*, 7958.
[67] X. Deng, Y. Yang, L. Wang, X. Z. Fu, J. L. Luo, *Adv. Sci.* **2021**, *8*, 2004523.